# Time-Domain Spectral Inversion Method for Characterization of Subsurface Layers in Ground-Penetrating-Radar (GPR) Applications

**Zohre Motevalli and Bijan Zakeri**

Department of Electrical and Computer Engineering
Babol Noshirvani University of Technology, Babol, Iran
zohre.dmt@gmail.com, zakeri@nit.ac.ir

***Abstract*** ─ Ground-Penetrating-Radar (GPR) data analysis has been widely utilized in subsurface and geophysics applications. One of the applications turning into great importance is multilayer subsurface hydraulic parameter identification and soil water content estimations. The classic GPR techniques have shown limitations in detecting deeper soil layers and unsatisfactory accuracy in estimating the electrical properties of the layers. Spectral inversion methods have been recently identified and developed to be an effective tool to tackle these problems. In this work, the spectral inversion method is extended in time-domain and a comprehensive formulation of the algorithm along with an improved well-defined cost function is presented. The Time-Domain Spectral Inversion (TDSI) method is then applied to environmentally-relevant multilayer soil geometries and the corresponding estimated electrical properties are drawn. The results show the TDSI method considerably ameliorates the performance of the inversion in terms of simplicity, accuracy, and applicability.

***Index Terms*** ─ Ground-Penetrating-Radar (GPR), microwave imaging, multilayer subsurface characterization, noise, soil moisture, Time-Domain Spectral Inversion (TDSI).

## I. INTRODUCTION

There are numerous methods to extract electrical properties of a material [1-4]. Among all existing methods, microwave imaging techniques including Synthetic Aperture Radar (SAR) [5], Time-Reversal (TR) [6, 7], and Ground-Penetrating-Radar (GPR) [8, 9] have become promising tools due to their non-destructive capabilities. These techniques rely on comparing the transmitted signals with the received ones. Moreover, choosing the best technique is primarily governed by the corresponding application. For instance SAR is prevalent for remote sensing applications [10] whereas GPR is employed for near-field subsurface characterizations [11]. Soil-based GPR constitutes countless activities in the fields of civil and construction [12], water resources [13], underground aquifers [14], and soil water content measurements [15]. GPR method is a function of soil's electrical parameters (electric permittivity, magnetic permeability, and conductivity), number of soil layers, and the performed survey method (e.g. Common Offset or Common Midpoint modes) [16]. More information regarding the principles and history of the GPR technique is covered by Jol [17].

Most of GPR techniques in the last decade for subsurface characterizations can be classified into four common categories: 1) Reflected Wave Velocity technique [18] identifies the dielectric constants by employing the wave velocity information and the corresponding propagation times reflected from the layers. 2) In Ground Wave technique [19], direct ground waves travel from the transmitting antenna to the receiving antenna just below the soil surface. The velocity of the direct ground wave is used to estimate the dielectric properties and the soil water content at shallow depths. 3) In Borehole Direct Wave Velocity technique [20], a transmitting and a receiving antenna are each separately placed in a nonmetallic tube. The tubes are then vertically deployed in the soil. Assuming the electromagnetic wave sent from the transmitter travels along a direct path through the soil to reach the receiver, and by knowing the line-of-sight distance between the transmitting and receiving antennas, the wave velocity is calculated. By knowing the wave velocity within the soil, the dielectric constant and the water content are derived. 4) Last not least, in Reflection Coefficient technique [21] two reflected waveforms from a flat soil surface and from a reference metallic layer are compared which eventually results in calculating the dielectric constant of the top surface layer. Ground Wave and Reflection Coefficient techniques yield the estimation of the top and shallow layers and are not capable of providing information for deeper layers [22]. The Borehole technique is also destructive and, in many cases, would not be feasible to excavate the soil. Furthermore, the main limitation of the aforementioned techniques arises from the fact that they almost employ partial information of the available data, either the propagation times or the reflection amplitudes. These techniques also suffer from

*Submitted On: January 12, 2017*
*Accepted On: December 24, 2018*

geometrical simplifications, such as ignoring the transceiver couplings and the distance from the soil's surface. The multiple reflections in soil layers are also not considered. To tackle the innate lack of data interpreting, a need for a new technique which considers the possible electromagnetic interactions seems desirable. Recently spectral inversion-based methods [22, 23] have shown promising results that would enable the utilization of the whole information of the data. The spectral inversion methods have also shown strong adaptability for thin layers [24]. Frequency-domain spectral inversion methods have been lately developed in terms of near-field wave modeling effects [25].

Even though the spectral inversion methods have been improved in recent years, most improvements have been achieved by defining the cost function in the frequency domain [26, 27]. Nonetheless, it is possible to have further improvements in the formulation, accuracy, and applicability of the method. With this goal, this paper presents formulations of Time-Domain Spectral Inversion (TDSI) method in presence of noise and exploits a well-defined cost function to ameliorate the performance of the method for multi-layer subsurface soil problems.

The remainder of the paper is organized as follows: In Section II the necessary formulations and theories behind a multilayer soil problem along with the details of TDSI method are introduced. In Section III, the specifications of the computational setup for synthetically-generated GPR data are explained. The results pertaining to the performance of TDSI method on environmentally-relevant soil geometries and in presence of noise are presented in Section IV and Section V, respectively. Finally, a summary of the present work and future contributions are drawn in Section VI.

## II. PROBLEM FORMULATION

In this section the necessary formulations and theories behind a multilayer soil problem are presented. The final formulation lays a foundation upon an improved TDSI method which will be performed for estimating the electrical properties of a three-layer soil problem.

### A. Generalized reflection coefficient

Figure 1 illustrates a semi-infinite two-dimensional *N*-layer model of multilayer soil geometry, where $\varepsilon_i$ is the relative permittivity, $\mu_i$ is the relative permeability, $\sigma_i$ is the conductivity, and $d_i = z_{i+1} - z_i$ is the thickness of each layer. The most fundamental modeling of such geometry is carried out by considering a homogeneous, linear, and isotropic medium. Moreover, the layers' interfaces are assumed to be non-rough. In the case the propagating wave with frequency *f* is plane and incident perpendicularly on the surface, the reflection $\Gamma$ and the transmission T coefficients corresponding to each interface are formulated as (1) and (2), respectively [28],

$$\Gamma_{i,i+1} = \frac{\eta_{i+1} - \eta_i}{\eta_{i+1} + \eta_i} \ , \tag{1}$$

$$\mathrm{T}_{i,i+1} = \frac{2\eta_{i+1}}{\eta_{i+1} + \eta_i} \ , \tag{2}$$

where $\eta_i$ is the characteristic impedance of each layer, and is written as (3),

$$\eta_i = \sqrt{\frac{j2\pi f \mu_0 \mu_i}{\sigma_i + j2\pi f \varepsilon_0 \varepsilon_i}} \ , \tag{3}$$

where $\varepsilon_0$=8.85×10$^{-12}$ (F/m) and $\mu_0$=1.26×10$^{-6}$ (H/m) are the vacuum permittivity and permeability, respectively. By solving the Maxwell's equations and applying the proper boundary conditions, the generalized reflection coefficient *R* looking from the top surface is formulated as (4)-(5) [28],

$$R = \frac{\Gamma_{12} + \tilde{\Gamma}_{23} e^{-2\gamma_2 d_1}}{1 + \Gamma_{12} \tilde{\Gamma}_{23} e^{-2\gamma_2 d_1}} \ , \tag{4}$$

$$\begin{aligned} \tilde{\Gamma}_{23} &= \frac{\Gamma_{23} + \tilde{\Gamma}_{34} e^{-2\gamma_3 d_2}}{1 + \Gamma_{23} \tilde{\Gamma}_{34} e^{-2\gamma_3 d_2}} \ , \\ &\vdots \\ \tilde{\Gamma}_{i,i+1} &= \frac{\Gamma_{i,i+1} + \tilde{\Gamma}_{i+1,i+2} e^{-2\gamma_{i+1} d_i}}{1 + \Gamma_{i,i+1} \tilde{\Gamma}_{i+1,i+2} e^{-2\gamma_{i+1} d_i}} \ , \end{aligned} \tag{5}$$

where $\gamma_i$ is the propagation constant of the *i*-th layer as formulated in (6),

$$\gamma_i = 2\pi f \sqrt{\mu_0 \mu_i \varepsilon_0 \varepsilon_i} \sqrt{1 - j \frac{\sigma_i}{2\pi f \varepsilon_0 \varepsilon_i}} \ . \tag{6}$$

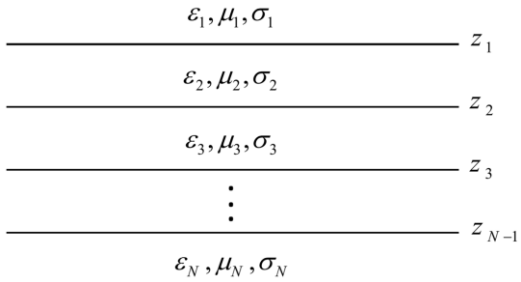


Fig. 1. Semi-infinite *N*-layer model of multilayer soil geometry.

For a three-layer model which will be conducted throughout this work the generalized reflection coefficient *R* can be obtained from (4)-(5) as (7),

$$R = \frac{\Gamma_{12} + \Gamma_{23} e^{-2\gamma_2 d}}{1 + \Gamma_{12} \Gamma_{23} e^{-2\gamma_2 d}} \ , \tag{7}$$

where *d* is the thickness of the middle soil layer. In

practical GPR applications, there is a close distance between the antenna transceivers and the top soil surface. The generalized reflection coefficient looking at the soil from the location of transceivers, therefore, needs to be corrected. If $h$ is the distance from the top soil layer and the transceivers, the corrected general reflection coefficient $R_c$ can be written as (8),

$$R_c = R e^{-2\gamma_1 h} = \frac{\Gamma_{12} + \Gamma_{23} e^{-2\gamma_2 d}}{1 + \Gamma_{12}\Gamma_{23} e^{-2\gamma_2 d}} e^{-2\gamma_1 h} . \quad (8)$$

Based on the corrected general reflection coefficient $R_c(f)$ and the incident waveform $F_x(f)$, the reflected waveform $F_y(f)$ back from the multilayer medium is calculated as (9),

$$F_y(f) = F_x(f) R_c(f) G(f) , \quad (9)$$

where $G(f)$ is the gain of the antenna. Assuming an isotropic radiation pattern with $G(f)$=1, (9) is simplified to (10),

$$F_y(f) = F_x(f) R_c(f) . \quad (10)$$

The next step to initiate the Time-Domain Spectral Inversion (TDSI) method is to convert the frequency-domain signal waveform (10) into a time-domain signal waveform. This can be performed by means of Inverse Fast Fourier Transform (IFFT). After modifying $R_c(f)$ and $F_x(f)$ to their proper conjugate double-side banded frequency-domain versions, the time-domain reflected waveform $f_y(t)$ can be represented as (11),

$$f_y(t) = \int_{-\infty}^{+\infty} F_x(f) \left[ \frac{\Gamma_{12} + \Gamma_{23} e^{-2\gamma_2 d}}{1 + \Gamma_{12}\Gamma_{23} e^{-2\gamma_2 d}} \; e^{-2\gamma_1 h} \right] e^{j2\pi ft} df , \quad (11)$$

where $F_x(f)$ can be calculated by taking the Fast Fourier Transform (FFT) of the incident time-domain waveform $f_x(t)$ as in (12),

$$F_x(f) = \int_{-\infty}^{+\infty} f_x(t) e^{-j2\pi ft} dt . \quad (12)$$

**B. Time-Domain Spectral Inversion (TDSI) method**

The main concept behind TDSI method is to minimize a well-defined cost function O[$f_y(t)$, $g_y(t)$] to achieve the best estimate (closeness) of the actual reflected waveform $g_y(t)$ by using the modeled reflected waveform $f_y(t)$. The actual waveform $g_y(t)$ can be either calculated synthetically (by computational methods) or measured practically. It is worth mentioning that the minimization problem is within ill-posed and non-unique classes of inverse scattering problem. This means the modeled waveform could become very similar to the actual waveform, but providing an inaccurate estimate of the modeled parameters. Converging to an answer yielding the correct estimate of the parameters and minimizing the cost function simultaneously is challenging [27].

Before treating the cost function, rectangular time windows are executed on $g_y(t)$ to remove the leakage of the transmitted signal into the received waveform. The next step is to identify the propagation times corresponding to each layer interface. We have taken advantage of the Short-Time Fourier Transform (STFT) algorithm and applied it on $g_y(t)$ to obtain the time-frequency spectrum $\bar{g}_y(f,\tau)$ as:

$$\bar{g}_y(f,\tau) = \mathrm{STFT}\left[ g_y(t) \right] = \int_{-\infty}^{+\infty} g_y(t) w(t-\tau) e^{-j2\pi ft} dt , \quad (13)$$

where $w(t-\tau)$ is a window function and generally chosen as Hann or Gaussian window. At each time cell $\tau$, the maximum magnitude of the entire frequencies is calculated and plotted against $\tau$. The propagation time of each layer interface is then identified as an extrema point in this plot (demonstrated in Section IV). In three-layer model, there are two interfaces which correspond to the first $M_1$ and second $M_2$ extrema points in the time-frequency spectrum, respectively, as (14)-(15),

$$\left\{ t_{M_1}, t_{M_2} \right\} = t \left\{ \max_{1,2} \left| \mathrm{STFT}\left[ g_y(t) \right] \right| \right\} , \quad (14)$$

$$\left\{ t'_{M_1}, t'_{M_2} \right\} = t' \left\{ \max_{1,2} \left| \mathrm{STFT}\left[ f_y(t) \right] \right| \right\} . \quad (15)$$

The improved cost function of this work is formulated to prevent solutions from trapping in ill-posed answers. The cost function has been gradually modified through a variety of test cases to yield a robust and case-independent performance. Taking into account (11)-(15), the cost function is then expressed as (16),

$$\mathrm{O}\left[ f_y(t), g_y(t) \right] = \left( \sum_{i=1}^{N} L_3(t_i) \right)^2 L_4 L_5 , \quad (16)$$

where $L_1$, $L_2$, $L_3$, $L_4$, and $L_5$ are the functions calculated through (17)-(21). $L_1^{\max}$ and $L_2^{\max}$ are the maxima of $L_1$ and $L_2$ calculated within $t_1$ to $t_N$. $L_1$, $L_2$, and $L_3$ are formulated to evaluate the similarity between the modeled and actual waveforms. $L_4$ and $L_5$ also force the amplitude and corresponding time of the extrema points meet each other,

$$L_1(t_i) = f_y(t_i) - g_y(t_i) , \quad (17)$$

$$L_2(t_i) = \left| f_y(t_i) \right| - \left| g_y(t_i) \right| , \quad (18)$$

$$L_3(t_i) = \left[ \frac{L_1(t_i)}{L_1^{\max}} + \frac{L_2(t_i)}{L_2^{\max}} \right] + \frac{L_1(t_i) L_2(t_i)}{L_1^{\max} L_2^{\max}} , \quad (19)$$

$$L_4 = f_y\left(t'_{M_1}\right) - g_y\left(t_{M_1}\right) + f_y\left(t'_{M_2}\right) - g_y\left(t_{M_2}\right) , \quad (20)$$

$$L_5 = \left( t_{M_1} - t'_{M_1} \right)^2 + \left( t_{M_2} - t'_{M_2} \right)^2 . \quad (21)$$

In the following sections the TDSI method will be applied on synthetically generated GPR data for a three-layer subsurface soil problem and the corresponding results and discussion will be presented.

## III. COMPUTATIONAL SETUP

The computational geometry of a three-layer soil problem is shown in Fig. 2. The common offset (CO) GPR data have been synthesized using 2D GPRMax [29] free-commercial software, which simulates the electromagnetic fields based on finite-difference-time-domain (FDTD) method [30]. The 2D computational domain is gridded into dimensions X×Y=200×200 cm$^2$, with a uniform spatial discretization of Δx=Δy=Δ=5 mm. The value of Δ is so assigned to create at least 10 nodes per $\lambda_m$, where $\lambda_m$ denotes the wavelength (proportion to layers permittivity) corresponding to the maximum frequency content of the excitation signal. The maximum runtime is set sufficiently enough for the incident wave to travel from the source to the bottom end of the domain in a round trip. The boundary condition is also a perfectly matched layer (PML) to provide reflectionless truncation of the computation domain. The PML thickness is set to 10Δ at all four sides of the boundaries. A z-directed infinitesimal electric dipole plays as a transceiver and moves along the *x*-axis in 18 cm (36Δ) steps and linearly surveys the soil layers. The perpendicular distance $h$ from the transceivers to the top surface layer is 75 cm (150Δ).

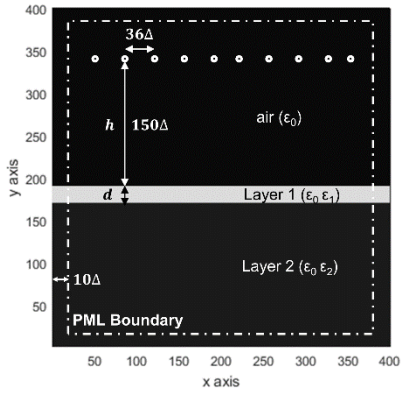


Fig. 2. Computational geometry (200×200 cm$^2$) of multilayer soil problem.

In this study twelve cases, six for each sandy and loamy soil cases with different volumetric water contents (VWC) [31] have been defined and evaluated by TDSI method, as shown in Table 1. The conductivity $\sigma$, however, is assumed constant and equal to 0.01 S/m for all cases.

The excitation signal is generally determined with respect to various constraints and specifications including particular electrical characteristics of the media, signal penetration through the soil layers, and portability of the setup [6]. To provide sufficient resolution for separating the layer responses in GPR data, a time-domain Ricker function (22) with proper adjusting parameters is considered as the excitation signal,

$$J(t) = -2\zeta\sqrt{e^{\frac{1}{2\zeta}}}\,e^{-\zeta(t-\chi)^2}(t-\chi), \qquad (22)$$

where $\zeta = 2\pi^2 f^2$, $\chi = 1/f$, and $f$ is the central frequency chosen as 2 GHz.

Minimization of the cost function O[$f_y(t)$,$g_y(t)$] in (16) was performed by means of Trust-Region-Reflective algorithm in Matlab ™ where the function takes the vector arguments $V_n = [\varepsilon_1, \varepsilon_2, d]^n$ in every iteration and returns a scalar value. The *finite-differential-relative-step* parameter of the algorithm also needs to be correctly adjusted to prevent the solutions from trapping in local optima.

Table 1: Sandy and loamy soil parameters. The conductivity $\sigma = 0.01$ S/m is constant for all cases

| | Sandy | | | Loamy | | |
|---|---|---|---|---|---|---|
| VWC (cm$^3$/cm$^3$) | $\varepsilon_1$ | $\varepsilon_2$ | $d$ (cm) | $\varepsilon_1$ | $\varepsilon_2$ | $d$ (cm) |
| 0.05 | 1.6 | 4.5 | 10 | 1.6 | 4.5 | 12.5 |
| 0.1 | 2.9 | 6.2 | 10 | 2.9 | 6 | 12.5 |
| 0.15 | 4.7 | 8.8 | 10 | 4.7 | 7.6 | 12.5 |
| 0.2 | 7.2 | 12 | 10 | 7.2 | 9.8 | 12.5 |
| 0.25 | 10.3 | 15.6 | 10 | 10.3 | 12.6 | 12.5 |
| 0.3 | 13.6 | 19.1 | 10 | 13.6 | 16.5 | 12.5 |

## IV. RESULTS

In this section the TDSI method is performed on the scenarios mentioned in the previous section. Fig. 3 represents a B-scan image of the loamy soil with VWC=0.15 cm$^3$/cm$^3$. The B-scan image is formed by collecting 10 A-scan traces of the linearly-surveyed GPR data. Each layer interface reflects a notable portion of the incident wave back to the transceiver. The interfaces are detectable as a bold line in the B-scan image. There are, however, a weaker trail of lines which may incorrectly be considered as additional interfaces. These trails are generally the consequence of near-field cylindrical wave propagation and multiple-reflections within the layers. The aforementioned problem can be tackled by exploiting STFT algorithm and the time-frequency spectrum as demonstrated in Fig. 4. The maximum magnitude of all frequencies at each time cell is plotted and shown in Fig. 4 (c). The extrema points (usually a threshold value is chosen) represent the time locations of the first and second actual interfaces, i.e., $t_{M_1}$ and $t_{M_2}$.

Following the formulations and methods described in Section II, the comparison between the synthetically-generated sample A-scan signal gy(t) (the fifth trace) and the estimated one fy(t) based on TDSI method is depicted in Fig. 5.

The estimated parameters, i.e., $\varepsilon_1$, $\varepsilon_2$, and $d$, by TDSI method for sandy soil and loamy soil along with the actual parameters for all VWC cases listed in Table 1 are illustrated in Fig. 6. As can be seen qualitatively the estimated values are within close agreement with the

actual values for both the sandy and loamy soil types. The results prove that the TDSI algorithm developed in this work is robust and its performance is case-independent. For the sandy soil, the average relative error between the estimated and actual values are calculated 3.70% for $d$, 9.01% for layer 1 relative permittivity $\varepsilon_1$, and 10.20% for layer 2 relative permittivity $\varepsilon_2$. For the loamy soil, the error values are calculated likewise as 5.43% for $d$, 12.94% for $\varepsilon_1$, and 13.88% for $\varepsilon_2$. The error values are ameliorated with respect to previous literature results [26, 27]. The GPR-based TDSI method also outperforms time-domain methods such as TR as it will not need the laborious data collection of time reversed array.

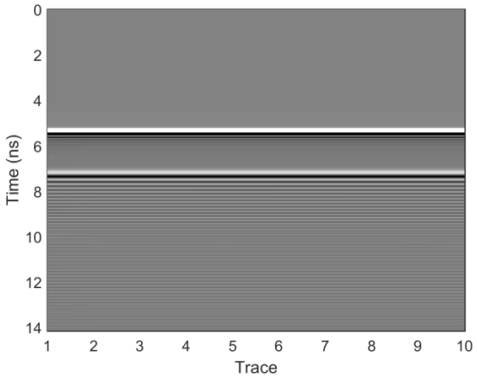


Fig. 3. B-scan image of 10 traces of linearly-surveyed GPR data for multilayer loamy soil with VWC=0.15 $cm^3/cm^3$. Each interface is displayed as a bold line in the B-scan image.

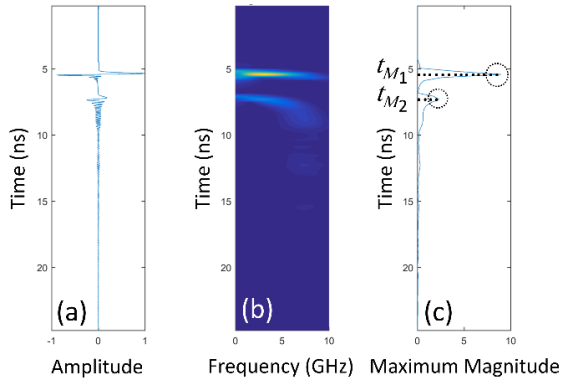


Fig. 4. Short-Time Fourier Transform (STFT) algorithm performed on a sample A-scan signal (the fifth trace) for the loamy soil with VWC=0.15 $cm^3/cm^3$. (a) A-scan signal, (b) time-frequency spectrum, and (c) magnitude-time plot. The extrema points and corresponding $t_{M_1}$ and $t_{M_2}$ are also shown.

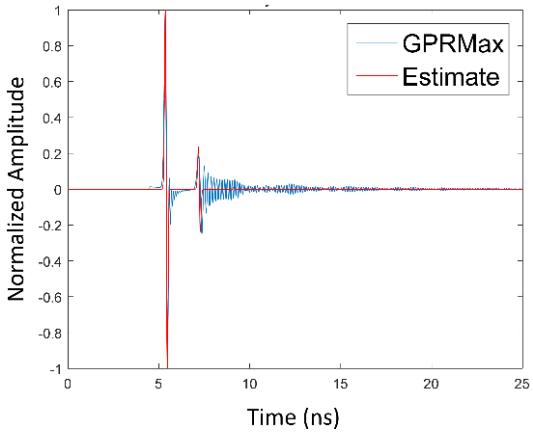


Fig. 5. Comparison of synthetically generated sample A-scan signal (the fifth trace) by GPRMax (blue) and the estimated one (red) using TDSI method for loamy soil with VWC=0.15 $cm^3/cm^3$.

## V. PRESENCE OF NOISE

In this section sandy soil with VWC=0.1 $cm^3/cm^3$ and loamy soil with VWC=0.25 $cm^3/cm^3$ have been chosen to evaluate the efficiency of TDSI method in presence of a random Gaussian noise with SNR=10 dB superimposed on the received signals. Figure 7 demonstrates the actual and estimated parameter values for the aforementioned soil types. According to Fig. 7 the relative permittivity values of the soil with higher VWC are overestimated. As VWC increases there is less contrast between the permittivity of layers (Table 1), therefore, the amplitude of the reflected waveform gets smaller and drowns below the noise level. This phenomenon influences the TDSI method as it yields overestimation of relative permittivity values.

## VI. CONCLUSION

In this work, a completed formulation of Time-Domain Spectral Inversion (TDSI) method was represented. The corresponding differential cost function was developed to a new well-defined function which was capable of minimizing the cost function and converging to a non-ill-posed answer representing a correct estimate of the parameters. The proposed TDSI method was then applied to twelve cases of environmentally-relevant three-layer sandy and loamy soil problems with different volumetric water contents. The results showed the estimated parameters were within a good agreement with the actual values and the calculated relative errors were substantially degraded and stood within appreciable tolerance compared to previous literature results.

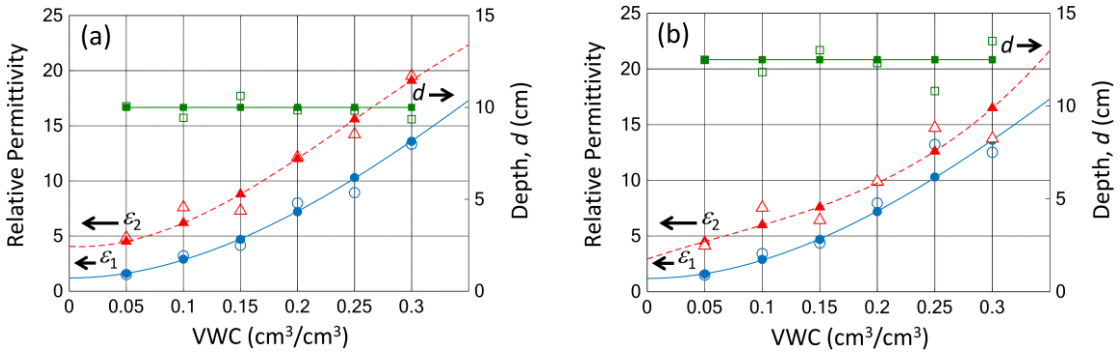


Fig. 6. Estimated (hollow symbols) and actual (filled symbols) parameter values of three-layer: (a) sandy and (b) loamy soil based on TDSI method. Solid lines are cubic fitted polynomial.

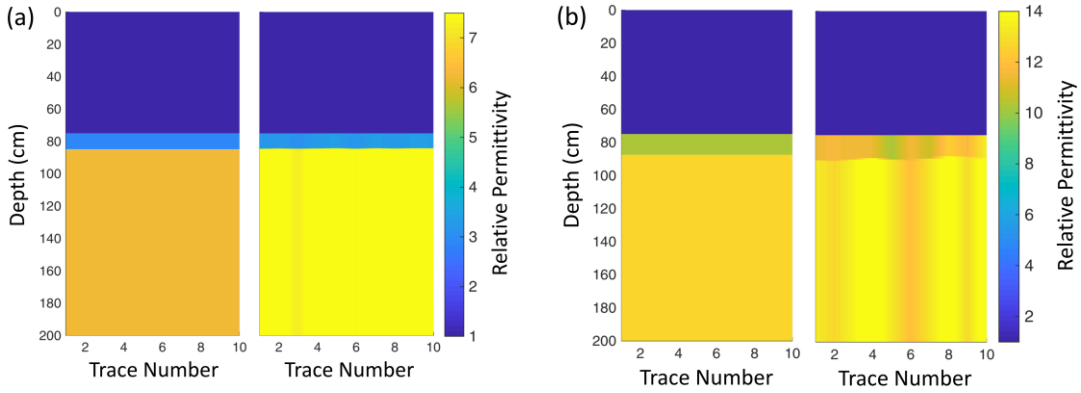


Fig. 7. Comparison of actual parameter values (left) and estimated values (right) based on TDSI method in presence of a 10 dB Gaussian noise for: (a) sandy soil with VWC=0.10 cm³/cm³, and (b) loamy soil with VWC=0.25 cm³/cm³.

## ACKNOWLEDGMENT

The authors would like to thank the reviewers for their valuable comments. The authors gratefully acknowledge Amin Gorji from Iowa State University, USA, for his support and knowledge in this project.

## REFERENCES

[1] M. Ozturk, U. K. Sevim, O. Akgol, E. Unal, and M. Karaaslan, "Determination of physical properties of concrete by using microwave nondestructive techniques," *Applied Computational Electromagnetics Society Journal*, vol. 33, 2018.

[2] A. Gorji and N. Bowler, "Dielectric measurement of low-concentration aqueous solutions: assessment of uncertainty and ion-specific responses," *Measurement Science and Technology*, 2018.

[3] J.-S. Lee, W.-T. Hong, K. Park, S. Hong, S.-H. Lee, and Y.-H. Byun, "Evaluation of water content in an active layer using penetration-type time domain reflectometry," *Applied Sciences*, vol. 8, p. 935, 2018.

[4] A. Elboushi, A. R. Sebak, and T. Denidni, "Through wall gap detection using monostatic radar," *Applied Computational Electromagnetics Society Journal*, vol. 28, 2013.

[5] C. Thajudeen, W. Zhang, and A. Hoorfar, "Efficient forward modeling of large scale buildings and through-the-wall radar imaging scenarios," *28th Annual Review of Progress in Applied Computational Electromagnetics (ACES)*, pp. 122-126, 2012.

[6] A. B. Gorji and B. Zakeri, "Time-reversal through-wall microwave imaging in rich scattering environment based on target initial reflection method," *Applied Computational Electromagnetics Society Journal*, vol. 30, 2015.

[7] S. Sadeghi and R. Faraji-Dana, "A practical UBE microwave imaging system using time-domain DORT for tumor detection," *Applied Computational Electromagnetics Society Journal*, vol. 31, 2016.

[8] K. Prokopidis and T. Tsiboukis, "Modeling of ground-penetrating radar for detecting buried objects in dispersive soils," *Applied Computational Electromagnetics Society Journal*, vol. 22, p. 287, 2007.

[9] S. MakalYucedag and A. Kizilay, "Time domain

analysis of ultra-wide band signals from buried objects under flat and slightly rough surfaces," in *ACES*, p. 646, 2013.

[10] B. K. Hornbuckle, J. C. Patton, A. VanLoocke, A. E. Suyker, M. C. Roby, V. A. Walker, *et al.*, "SMOS optical thickness changes in response to the growth and development of crops, crop management, and weather," *Remote Sensing of Environment*, vol. 180, pp. 320-333, 2016.

[11] D. Comite, A. Galli, I. Catapano, and F. Soldovieri, "Advanced imaging for down-looking contactless GPR systems," in *Applied Computational Electromagnetics Society Symposium-Italy (ACES) International*, 2017, pp. 1-2, 2017.

[12] Z. W. Wang, M. Zhou, G. G. Slabaugh, J. Zhai, and T. Fang, "Automatic detection of bridge deck condition from ground penetrating radar images," *IEEE Transactions on Automation Science and Engineering*, vol. 8, pp. 633-640, 2011.

[13] H. Liu, K. Takahashi, and M. Sato, "Measurement of dielectric permittivity and thickness of snow and ice on a brackish Lagoon using GPR," *IEEE Journal of Selected Topics in Applied Earth Observations and Remote Sensing*, vol. 7, pp. 820-827, 2014.

[14] H. Liu, X. Xie, J. Cui, K. Takahashi, and M. Sato, "Groundwater level monitoring for hydraulic characterization of an unconfined aquifer by common mid-point measurements using GPR," *Journal of Environmental and Engineering Geophysics*, vol. 19, pp. 259-268, 2014.

[15] L. Weihermüller, J. Huisman, S. Lambot, M. Herbst, and H. Vereecken, "Mapping the spatial variation of soil water content at the field scale with different ground penetrating radar techniques," *Journal of Hydrology*, vol. 340, pp. 205-216, 2007.

[16] R. W. Jacob and T. Urban, "Ground-penetrating radar velocity determination and precision estimates using common-midpoint (CMP) collection with hand-picking, semblance analysis and cross-correlation analysis: A case study and tutorial for archaeologists," *Archaeometry*, vol. 58, pp. 987-1002, 2016.

[17] H. M. Jol, *Ground Penetrating Radar Theory and Applications*. Elsevier, 2008.

[18] Y. Nakashima, H. Zhou, and M. Sato, "Estimation of groundwater level by GPR in an area with multiple ambiguous reflections," *Journal of Applied Geophysics*, vol. 47, pp. 241-249, 2001.

[19] L. Galagedara, G. Parkin, J. Redman, P. Von Bertoldi, and A. Endres, "Field studies of the GPR ground wave method for estimating soil water content during irrigation and drainage," *Journal of Hydrology*, vol. 301, pp. 182-197, 2005.

[20] D. F. Rucker and T. Ferré, "Near-surface water content estimation with borehole ground penetrating radar using critically refracted waves," *Vadose Zone Journal*, vol. 2, pp. 247-252, 2003.

[21] G. Serbin and D. Or, "Ground-penetrating radar measurement of soil water content dynamics using a suspended horn antenna," *IEEE Transactions on Geoscience and Remote Sensing*, vol. 42, pp. 1695-1705, 2004.

[22] S. Lambot, E. C. Slob, I. van den Bosch, B. Stockbroeckx, and M. Vanclooster, "Modeling of ground-penetrating radar for accurate characterization of subsurface electric properties," *IEEE Transactions on Geoscience and Remote Sensing*, vol. 42, pp. 2555-2568, 2004.

[23] C. I. Puryear and J. P. Castagna, "Layer-thickness determination and stratigraphic interpretation using spectral inversion: Theory and application," *Geophysics*, vol. 73, pp. R37-R48, 2008.

[24] J. Minet, S. Lambot, E. C. Slob, and M. Vanclooster, "Soil surface water content estimation by full-waveform GPR signal inversion in the presence of thin layers," *IEEE Transactions on Geoscience and Remote Sensing*, vol. 48, pp. 1138-1150, 2010.

[25] A. P. Tran, F. Andre, and S. Lambot, "Validation of near-field ground-penetrating radar modeling using full-wave inversion for soil moisture estimation," *IEEE Transactions on Geoscience and Remote Sensing*, vol. 52, pp. 5483-5497, 2014.

[26] Y. Huang, J. Zhang, and J. Chen, "Application of time-frequency domain spectral decomposition based on least-square matching pursuit to improve subsurface imaging," in *29th Annual Review of Progress in Applied Computational Electromagnetics*, Monterey, CA, USA, 2013.

[27] Z.-l. Huang and J. Zhang, "Determination of parameters of subsurface layers using GPR spectral inversion method," *IEEE Transactions on Geoscience and Remote Sensing*, vol. 52, pp. 7527-7533, 2014.

[28] W. C. Chew, *Waves and Fields in Inhomogeneous Media*. vol. 522: IEEE Press New York, 1995.

[29] A. Giannopoulos, "Modelling ground penetrating radar by GPRMax," *Construction and Building Materials*, vol. 19, pp. 755-762, 2005.

[30] A. Taflove and S. Hagness, *Computational Electrodynamics: The Finite-Difference Time Domain Method*. 3rd ed., Artech House Boston, 2005.

[31] J. Cihlar and F. T. Ulaby, "Dielectric properties of soils as a function of moisture content," 1974.